

On the scalability of helium-filled soap bubbles for volumetric PIV

Grille Guerra, A.; Scarano, F.; Sciacchitano, A.

Publication date

2024

Document Version

Final published version

Published in

Experiments in Fluids: experimental methods and their applications to fluid flow

Citation (APA)

Grille Guerra, A., Scarano, F., & Sciacchitano, A. (2024). On the scalability of helium-filled soap bubbles for volumetric PIV. *Experiments in Fluids: experimental methods and their applications to fluid flow*, 65(23).

Important note

To cite this publication, please use the final published version (if applicable). Please check the document version above.

Copyright

Other than for strictly personal use, it is not permitted to download, forward or distribute the text or part of it, without the consent of the author(s) and/or copyright holder(s), unless the work is under an open content license such as Creative Commons.

Takedown policy

Please contact us and provide details if you believe this document breaches copyrights. We will remove access to the work immediately and investigate your claim.



On the scalability of helium-filled soap bubbles for volumetric PIV

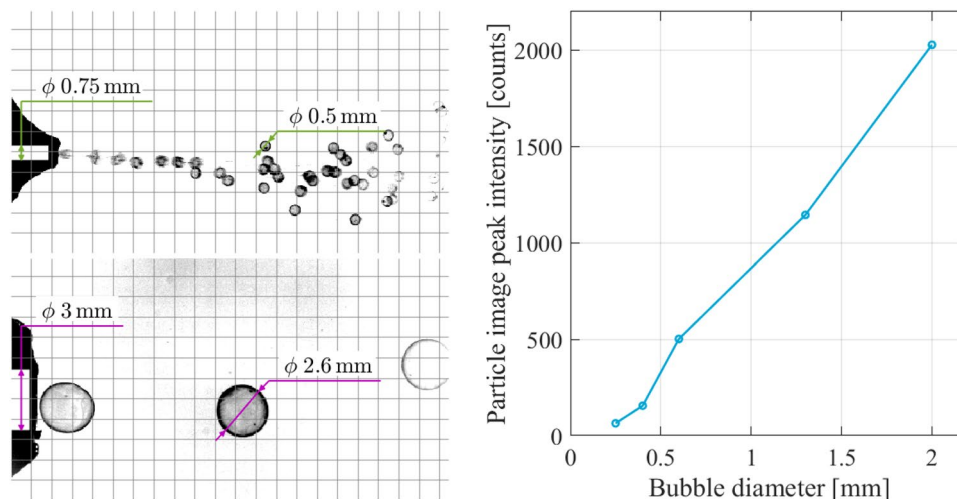
Adrian Grille Guerra¹ · Fulvio Scarano¹ · Andrea Sciacchitano¹

Received: 14 September 2023 / Revised: 3 December 2023 / Accepted: 2 January 2024 / Published online: 4 February 2024
© The Author(s) 2024

Abstract

The scalability of experiments using PIV relies upon several parameters, namely illumination power, camera sensor and primarily the tracers light scattering capability. Given their larger cross section, helium-filled soap bubbles (HFSB) allow measurements in air flows over a significantly large domain compared to traditional oil or fog droplets. Controlling their diameter translates into scalability of the experiment. This work presents a technique to extend the control of HFSB diameter by geometrical variations of the generator. The latter expands the more limited range allowed by varying the relative helium-air mass flow rates. A theoretical model predicts the bubble size and production rate, which is verified experimentally by high-speed shadow visualization. The overall range of HFSB produced in a stable (*bubbling*) regime varies from 0.16 to 2.7 mm. Imaging by light scattering of such tracers is also investigated, in view of controversies in the literature on whether diffraction or geometrical imaging dominate the imaging regime. The light scattered by scaled HFSB tracers is imaged with a high-speed camera orthogonal to the illumination. Both the total energy collected on the sensor for a single tracer, as well as its peak intensity, are found to preserve scaling with the square of the diameter at object magnification of 10^{-1} or below, typical of PIV experiments. For large-scale volumetric applications, it is shown that varying the bubble diameter allows increasing both the measurement domain as well as the working distance of the imagers at 10 m and beyond. A scaling rule is proposed for the latter.

Graphical abstract



✉ Adrian Grille Guerra
a.grilleguerra@tudelft.nl

¹ Faculty of Aerospace Engineering, Delft University of Technology, Delft, The Netherlands

1 Introduction

Volumetric velocity measurements have enabled a significant step forward in the fundamental understanding of complex three-dimensional flows, including turbulence (Westerweel

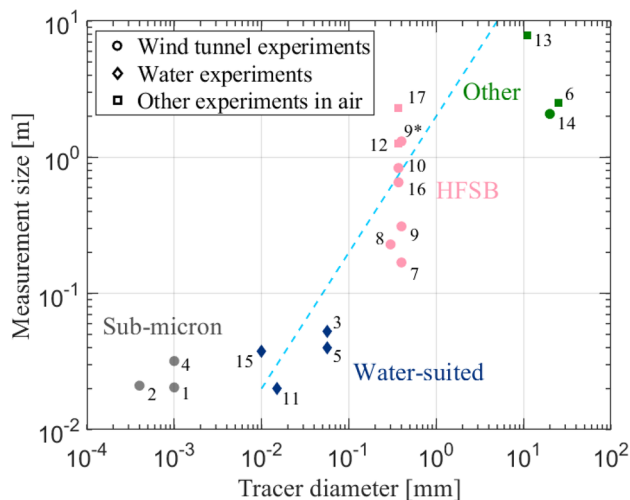


Fig. 1 Measurement size of PIV experiments versus tracer diameter. Experiments are sorted according to the year of publication. 1 Elsinga et al. (2006), 2 Humble et al. (2009), 3 Scarano and Poelma (2009), 4 Atkinson et al. (2011), 5 Schröder et al. (2011), 6 Rosi et al. (2014), 7 Scarano et al. (2015), 8 Caridi et al. (2016), 9* Jux et al. (2018), 10 Schanz et al. (2019), 11 Tokgoz et al. (2020), 12 Godbersen et al. (2021), 13 Wei et al. (2021), 14 Hou et al. (2021), 15 van Hout et al. (2022), 16 van der Hoek et al. (2022) and 17 Schröder et al. (2022). *The total measurement volume combines several views from robotic PIV

et al. 2013). After the introduction of tomographic PIV (Elsinga et al. 2006), many volumetric experiments were realised both in air and water flows (Scarano 2013). Yet, the domain that could be covered remained in the order of 10^1 – 10^2 cm³, mostly due to the unfavourable scaling of the volume size and the particle detectability. For air flows, the set-up typically involved expanding a Nd/YAG laser beam to illuminate a thicker plane. Concurrently, the imaging system needed to encompass such a thickness within its focal depth. Using the typical seeding tracers of 1 μ m diameter, experiments rarely exceeded a volume thickness of 1 cm (Atkinson et al. 2011; Humble et al. 2009, among others). This restriction is partly relaxed in water flow experiments, where neutrally buoyant tracers of larger size can be employed. For example, 10 μ m hollow glass spheres were frequently employed (van Hout et al. 2022), 15 μ m Rhodamine B particles (Tokgoz et al. 2020) or most frequently 56 μ m polyamide particles (Schröder et al. 2011; Percin and van Oudheusden 2015; Scarano and Poelma 2009) have also been employed for measurement volumes exceeding 100 cm³. Upscaled field-experiments adopted solutions such as snow-flakes as natural tracers (Wei et al. 2021), however, with limited control of their concentration and tracing fidelity.

A major leap forward in terms of upscaling was introduced by developing large neutrally buoyant tracers techniques based on helium-filled soap bubbles (HFSB) as PIV tracers (Bosbach et al. 2009). Early applications of HFSB

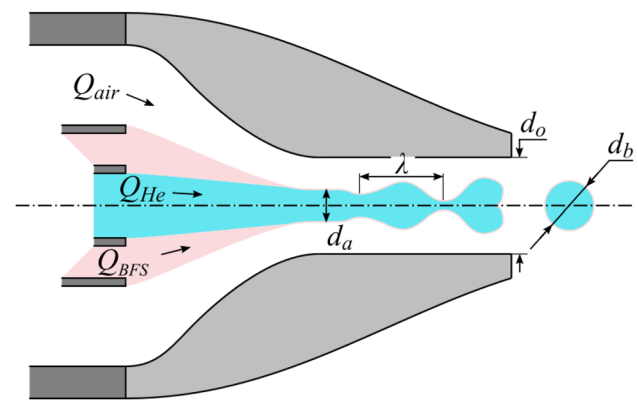


Fig. 2 Schematic illustration of a HFSB generator exit region

in aerodynamics were made for flow visualization (Hale et al. 1971) and the low production rate of bubble generators (typically below 1000 bubbles/s, <http://www.sageaction.com>) discouraged their application for PIV measurements in wind tunnels. Furthermore, the work from Kerho and Bragg (1994) indicated that HFSB in the millimetre range were unsuited for the study of aerodynamic flows. Later, at the German Aerospace Centre (DLR) a miniature generator was developed, capable of producing 230 μ m HFSB at a rate of 200,000 bubbles/s (Bosbach et al. 2009). The aerodynamic behaviour of sub-millimetre HFSB tracers was again evaluated and compared to conventional fog droplets, yielding a Stokes response time in the order of 10–30 μ s (Faleiros et al. 2018), thus proving the suitability of HFSB for low-speed aerodynamics experiments.

An early HFSB seeding system for wind tunnels involved the accumulation and rapid release of bubbles inside a piston-cylinder device, operating a single or very few generators (Caridi et al. 2016). Coupling a generator with a piston-cylinder system to accumulate the tracers, Scarano et al. (2015) introduced HFSB at a higher rate in a wind tunnel within a volume of approximately 5 L. However, this approach required large ducts for transport and dispersion, disturbing the free stream uniformity and turbulence intensity. The latter piston-cylinder system was superseded by systems featuring arrays of tens (Gibeau et al. 2020) or hundreds of generators (Scarano et al. 2022). Using a 204-generators seeder, Van Der Hoek et al. (2022) measured the wake of a scaled horizontal-axis wind turbine over a volume of 280 L. At the Netherlands Aerospace Laboratories (NLR), an array of 3×3 m² comprising 400 generators was operated to measure the velocity field around a tilt-rotor model aircraft over 0.7 m³ (Faleiros 2021). Finally, the use of HFSB for indoor ventilation (Bluyssen et al. 2021; Kühn et al. 2011) and on-site aerodynamics (Spoelstra et al. 2019) has sparked interest in further upscaling of experiments.

The scattered light of HFSB has been reported to largely exceed that of conventional micron-size PIV tracers, namely 10^4 – 10^5 times (Caridi 2018). This corresponds with a scaling of the particle image peak intensity with the square of the particle diameter, in agreement with Mie theory of scattering, and an imaging regime governed by diffraction. The above is in contrast with the literature, where such scaling has been long questioned. Just to cite the two most popular books on PIV (Adrian and Westerweel 2011; Raffel et al. 2018), it is conjectured that beyond a given tracer size (assumed around $100\ \mu\text{m}$), the increase in scattered light would not increase the particle image peak intensity and therefore not improve the particle detectability (Adrian 1991). In the present work, the optical properties of HFSB tracers are reviewed, and the parameters governing the scaling of particle peak intensity are investigated, to a conclusive clarification on the subject.

From an experimental perspective, the difference in scattering power justifies the large difference in the size (reference length scale from the reported measurement volume) of experiments conducted with conventional PIV tracers in air (Fig. 1 grey cluster) and those making use of HFSB (pink cluster). Overall, the measurement size is found to correlate linearly with the particle tracer diameter, which is further discussed in the remainder of this study.

Despite the interest in experiment upscaling or downscaling (see for instance the work from Barros et al. 2021), the survey of most experiments performed in the past decade shows that HFSB tracers have been used in a relatively narrow range of diameters, namely between 0.3 and 0.6 mm as allowed by the fine control of the relative helium-air flow rates, as discussed in the seminal study by Faleiros et al. (2019). Beyond a specific range of *bubbling* production, the generator was reported to either interrupt production or to enter some irregular regimes with a much broader range of sizes and less controlled neutral buoyancy condition. The above work concluded that for a given generator, a max–min ratio (MMR) of bubble diameters not exceeding 1.5 could be practically achieved. The present work revises the main hypothesis of constant generator geometry, in the attempt to significantly extend the MMR for the benefit of measurement upscaling (or downscaling). By doing so, one responds to experimental needs on two sides: at first, smaller tracers enable volumetric experiments at medium scale (approx. 1 L) of fundamental problems (e.g. jets, boundary layers, wakes); secondly, larger tracers will extend further the range of large-scale PIV (several cubic metres) for full-scale on-site applications. Examples of the latter were made in the automotive sector (Hüttig et al. 2023) and for sport aerodynamics (Jux et al. 2018).

The first part of this study reviews the working principle of the HFSB generator, based on the supply of helium,

bubble fluid solution (BFS) and air, to complete the description of the bubble generation process. Furthermore, the scaling behaviour based on gas flow rates and on exit orifice variation is discussed, both using a developed theoretical model and also bubble visualization experiments. It is shown that production of neutrally buoyant HFSB is possible in the range of diameters 0.16–2.7 mm.

The second part of the study focuses on the impact of the tracer size to the image properties. A theoretical model is proposed and discussed first, followed by light scattering experiments to confirm the validity of the hypothesis considered. It is shown that increasing the bubble diameter allows increasing both the measurement domain as well as the working distance of the imagers to 10 m and beyond. Finally, a best-practice criterion is proposed for the selection of the adequate tracer size for a given volumetric PIV experiment.

2 Working principle of HFSB generation

The working principle of a generic HFSB generator is sketched in Fig. 2. Helium (light blue) exits from the inner duct, surrounded by a ring-shaped duct supplying the bubble fluid solution (BFS, in pink). On the outer ring, the air flow has two main functions: (1) the air flow act as a buffer (avoiding contact) between the soap film and the outer surface of the duct. As a result, it becomes possible to converge the streamlines and reduce the size of the bubbles; (2) the air flow, similar to that of helium acts on the outer side of the BFS flow and the shear force results in its acceleration and thinning. This effect is important to obtain a thin BFS film such to attain neutral buoyancy of the bubble. A fluid supply unit (FSU) provides the desired helium, BFS and air volume flow rates (Q_{He} , Q_{BFS} and Q_{air} , respectively), while the conditions at the exit are dictated by the orifice diameter, d_o .

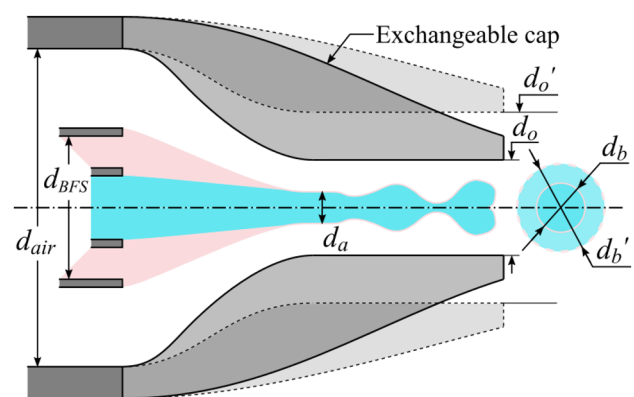


Fig. 3 Schematic illustration of a scalable HFSB generator, where an exchangeable cap is used to change the orifice diameter from d_o to d_o' , thus yielding a variation of the bubbles diameters from d_b to d_b'

From the visualization studies of Faleiros et al. (2019), it emerges that HFSB achieve a spherical shape a few diameters after release from the orifice. This allows expressing the bubble volume V_b simply as:

$$V_b = \frac{\pi}{6} d_b^3, \tag{1}$$

where d_b is the bubble diameter. The bubble volume is composed of helium and a thin layer (less than a micrometre, Kerho and Bragg 1994) of BFS. In the hypothesis that the helium gas is not lost during the production of bubbles, a simple estimate of the HFSB production frequency f_p is obtained on the basis of the helium flow rate and the bubble volume V_b as:

$$f_p = \frac{Q_{He}}{V_b}. \tag{2}$$

The production mechanism is explained here in the following hypotheses: air, helium and BFS reach the same velocity at the exit orifice (Mu et al. 2020); air and helium maintain approximately equal pressure (except for the pressure difference caused by the soap film tension) along the contraction; BFS is released at the lip of the inner tubes continuously at a negligible velocity compared to that of the gases. The released BFS is extruded under the shearing action of the helium and air flows. The work done by the shear stresses at the helium-BFS and air-BFS interfaces accelerates the BFS film. As a result of mass conservation, its thickness is reduced and the surface area is increased. At the end of the nozzle contraction, the BFS flow features a thin annular shape of diameter d_a . In the above hypotheses, d_a can be derived from the air-to-helium ratio of flow rates and the orifice diameter:

$$d_a = d_o \left(1 + \frac{Q_{air}}{Q_{He}} \right)^{-1/2}. \tag{3}$$

The annular BFS film is subject to Plateau–Rayleigh instability (Rayleigh 1878), whereby disturbances of varicose mode are amplified eventually leading to the breakdown of the BFS filament into bubbles. The most amplified wavelength, λ , dictates the final bubble diameter as well as the

production rate. Rayleigh (1878) derived theoretically the value of such wavelength for a cylindrical liquid jet in air, obtaining $\lambda \approx 4.5d_a$. In absence of a theoretical value of λ for a hollow liquid film, we will use the latter value as first estimate for the most amplified wavelength. At the nozzle exit, due to the conservation of the helium mass, the cylinder of length λ and diameter d_a transforms into a spherical bubble of diameter d_b :

$$\frac{\pi}{4} \lambda d_a^2 = \frac{\pi}{6} d_b^3. \tag{4}$$

Introducing this relation and the estimate for λ in Eq. (3) finally yields a theoretical estimate of the bubble diameter as:

$$d_b \approx 1.9d_o \left(1 + \frac{Q_{air}}{Q_{He}} \right)^{-1/2}. \tag{5}$$

The above equation shows that the bubble diameter depends linearly upon the orifice diameter and in a milder way (0.5 exponent) upon the ratio of gases flow rates. The latter has been practised and reported in several past experiments (Faleiros et al. 2019; Gibeau and Ghaemi 2018). However, it was also observed that controlled production of HFSB only occurs in a limited range of values for such ratio. For instance, Faleiros et al. (2019) showed that at too low air flow rate, the generator produces irregular bubbles of disperse diameter. Furthermore, at too high values of Q_{air} , the annular BFS film breaks up downstream of the orifice (*jetting* regime), leading to a polydisperse bubble generation. As a result, the ratio Q_{air}/Q_{He} for controlled production of monodispersed bubbles needs to be limited approximately between 5 and 15. Using Eq. (5), this would result in a max–min ratio of bubble diameter of 1.6, with bubble diameters typically between 0.45 and 0.8 times the orifice diameter. Current experiments, along with those reported by Faleiros et al. (2019) or Gibeau and Ghaemi (2018) confirm such range limitations.

2.1 Scalable HFSB generation

The present work explores the control of HFSB size by altering the orifice diameter d_o and the flow rates of the supply fluids, while maintaining unaltered the geometry upstream of the contraction (see Fig. 3). In the simplifying hypothesis of equal pressure and velocity of the helium and air streams at the exit of the coaxial duct, the soap film contracts from the initial diameter d_{BFS} to d_a following the geometrical contraction of d_{air}/d_o . It can be concluded that small bubbles can be obtained by miniaturizing the coaxial tube or by reducing the exit orifice. The former option is technically challenging, considering that current systems already feature a coaxial duct in the order of 1 mm and a wall thickness of the coaxial

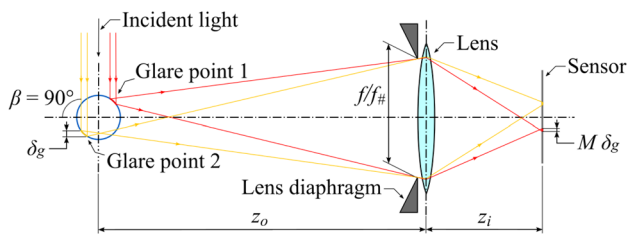


Fig. 4 Sketch of the illumination and imaging of a HFSB

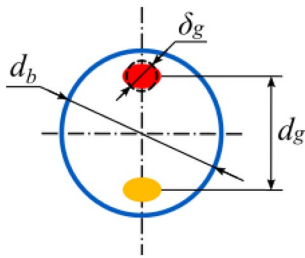


Fig. 5 Sketch of the glare points of a HFSB in the object space

ducts in the order of 0.2 mm, at the limit of manufacturing accuracy or 3D printing. The latter option, instead, only requires a modification of the orifice diameter, currently in the order of 1 mm.

3 Light scattering behaviour of HFSB

HFSB have been introduced for their increased light scattering capabilities compared to conventional fog droplets. While it is clear that bigger particles scatter more light due to the larger cross section, the light reflecting region spreads over an area larger than the wavelength of the incident light and therefore entering the geometrical reflection regime. When such region is also resolved geometrically in the image, the particle image peak intensity reaches a plateau. This principle has been discussed in the early work of Adrian and Yao (1985), who, however, extrapolated their conclusions from conditions of high magnification, ultimately leading to the misconception of an upper bound for the tracers size. The main point of discussion is whether increasing the size of tracers, HFSB in particular, experiments at larger scale and/or at larger illumination and imaging distance can be performed. A discussion is developed hereafter that aims at determining the governing parameters of this optical problem and identifying the regimes for PIV experiments at different scales. Let us consider a measurement volume V (a cube of length L for simplicity) seeded with HFSB tracers illuminated and imaged with a 3D PIV system. The illumination, light reflection and imaging situation are schematically represented in Fig. 4. The light scattered by the bubble is collected at a distance z_0 by a lens of focal length f and numerical aperture $f_\#$, whereas z_i is the lens-sensor distance. As discussed by Adrian (1991) for planar PIV, the energy collected over the area of a particle image, $\bar{\epsilon}$, is given by:

$$\bar{\epsilon} \sim \underbrace{\frac{I_0}{L^2}}_{\text{Illumination}} \cdot \underbrace{\lambda_0^2 \left(\frac{d_b}{\lambda_0}\right)^n}_{\text{Light scattering}} \cdot \underbrace{\left(\frac{f/f_\#}{z_0^2 d_\tau^2}\right)^2}_{\text{Imaging}} \tag{6}$$

where I_0 and λ_0 are the pulse energy and wavelength of the incident light, n is the power-law exponent describing the scattered light energy and d_τ is the particle image diameter. The right-hand side of Eq. (6) has been rearranged into three different factors that account for the contribution of illumination, light scattering and imaging, respectively.

3.1 Illumination

The original derivation of Eq. (6) is based on laser illumination (monochromatic, collimated and coherent) as commonly employed for PIV. For volumetric illumination, the energy of the light pulse needs to be spread over the width and height of the laser sheet, thus scaling as $1/L^2$. For uncollimated light sources, such as LEDs, the energy flux depends on the relative distance between the light source and the tracer. In general, LED illuminators are placed at a distance from the measurement volume that is comparable to the size of this volume itself. This is done to achieve to best compromise between light intensity evenness across the volume and total energy flux. In this situation, the same scaling as for collimated light sources applies. In the present discussion, collimated illumination from a single direction is considered, for sake of simplicity.

3.2 Light scattering

The light scattered from a spherical particle as a function of the particle diameter is described by Mie’s theory (Hergert and Wriedt 2012). The relative diameter of the particle (d_p) to the wavelength of the illumination demarcates the range of Rayleigh ($d_p \ll \lambda_0$), Mie ($d_p \sim \lambda_0$) and geometric scattering ($d_p \gg \lambda_0$), respectively. Conventional PIV seeding (liquid droplets around 1 μm) lies in the intermediate Mie region. For Rayleigh scattering, the power-law exponent tends to $n = 6$, while this drops to $n = 2$ for geometric scattering (Tropea 2011), which is the case for HFSB.

For particles in the Mie region, the scattered light intensity strongly depends on the angle between the illuminator and the camera (Raffel et al. 2018), β , which is therefore of utter importance for PIV experiments. Conversely, previous results from Caridi (2018) have demonstrated only minor variations for the case of HFSB, which is a direct consequence of these pertaining to the geometric scattering regime. For the sake of simplicity, side scattering ($\beta = 90^\circ$) is considered in the remainder of the document.

In the geometric scattering regime, the various scattering orders (e.g. reflection and refraction) can be visualized

Table 1 Survey of large-scale experiments performed with tracers in the mm–cm range

Research group	Measurement volume, V (reference length scale, $L = \sqrt[3]{V}$)	Tracers (d_b)	d_b/L	$R_{GD} = \frac{M\delta_g}{d_{diff}}$	$R_{DD} = \frac{Md_g}{d_{diff}}$
Rosi et al. (2014), atmospheric boundary layer	16 m ³ (2.5 m)	Fog-filled soap bubbles (25 mm)	10 ⁻²	4 × 10 ⁻³	Not applicable
Scarano et al. (2015), cylinder wake	4.8 × 10 ⁻³ m ³ (0.17 m)	HFSB (0.4 mm)	10 ⁻³	10 ⁻³	0.6
Caridi et al. (2016), vertical-axis wind turbine	1.2 × 10 ⁻² m ³ (0.23 m)	HFSB (0.3 mm)	10 ⁻³	6 × 10 ⁻⁴	0.7
Jux et al. (2018), full-scale cyclist	3 × 10 ⁻² m ³ (0.31 m)	HFSB (0.4 mm)	10 ⁻³	6 × 10 ⁻⁴	0.06
Schanz et al. (2019), turbulent boundary layer	5.8 × 10 ⁻¹ m ³ (0.83 m)	HFSB (0.37 mm)	4 × 10 ⁻⁴	2 × 10 ⁻⁴	0.3
Godbersen et al. (2021), Rayleigh-Bénard convection	2 m ³ (1.2 m)	HFSB (0.37 mm)	3 × 10 ⁻⁴	10 ⁻⁴	0.2
Wei et al. (2021), vertical-axis wind turbine	490 m ³ (7.9 m)	Artificial snow (11 mm)	10 ⁻³	6 × 10 ⁻⁴	Not applicable
Hou et al. (2021), tractor-trailer model	9 m ³ (2.1 m)	Air-filled soap bubbles (20 mm)	10 ⁻²	4 × 10 ⁻³	15
van der Hoek et al. (2022), horizontal-axis wind turbine	2.8 × 10 ⁻¹ m ³ (0.65 m)	HFSB (0.37 mm)	6 × 10 ⁻⁴	2 × 10 ⁻⁴	0.8
Schröder et al. (2022), breathing human model	12 m ³ (2.3 m)	HFSB (0.37 mm)	2 × 10 ⁻⁴	7 × 10 ⁻⁵	0.2

Size of tracers, corresponding measurement volume and their ratio. Non-dimensional parameter R_{GD} indicating ratio of glare to diffraction diameters. R_{DD} ratio of glare points distance to diffraction diameter

through simple ray-tracing models. Since the difference in refractive index between helium and air is negligible, and given the small thickness of the soap film, refraction is neglected in the present discussion.

3.3 Imaging

For volumetric PIV, two visible regions (the so-called glare points) are imaged per tracer, oriented along the illumination direction. A first visible region is caused by the light rays reflected at the bubble’s outer surface that are captured by the lens aperture. For HFSB, a second glare point appears from the light rays that initially go through the bubble before being reflected at the inner surface (see Fig. 4). The projection of these regions onto a plane parallel to the sensor indicates an elliptical shape of eccentricity $e = 1/\sqrt{2}$, as sketched in Fig. 5. To simplify the discussion, the size of the glare points is defined here based on an equivalent diameter (δ_g), obtained as the average between the axes of the ellipse. The glare point diameter in the object space depends not only on the bubble size but also on the imaging conditions, since these affect the subtended angle of light captured by the lens. As discussed by Faleiros et al. (2021), this may be approximated as:

$$\delta_g \approx \frac{2 + \sqrt{2} f d_b}{16 f_{\#} z_o} \tag{7}$$

The geometrical image of the glare points does further depend on the imaging configuration through the optical magnification, $M = z_i/z_o$, such that the imaged size becomes $M\delta_g$ (see Fig. 4). Another contribution to the glare point size in the image plane is due to diffraction, whereby a point source is imaged over a finite spot of diameter d_{diff} (Goodman 1996):

$$d_{diff} = 2.44\lambda_0 f_{\#}(1 + M). \tag{8}$$

Assuming both the geometric image and the point response function behave as a Gaussian distribution (Adrian and Yao 1985), the glare point image diameter (d_{τ}) can be approximated as:

$$d_{\tau} = \sqrt{(M\delta_g)^2 + d_{diff}^2}. \tag{9}$$

In the above expression, the effects of optical aberrations are neglected and the glare points are assumed to be imaged in focus. Furthermore, it is assumed that d_{τ} is larger than the sensor pixel, which allows neglecting the discretisation effects due to pixels. As the relative importance of geometric imaging and diffraction is still subject to the imaging conditions, a further relation can be obtained from the depth of focus. For volumetric PIV, it is crucial for the focal depth δZ to be larger or equal than the depth of the measurement volume L , leading to (Schuth and Buerakov 2017):

$$\delta Z = 2f_{\#}d_{\text{diff}} \frac{1+M}{M^2} \geq L. \tag{10}$$

Considering $\delta Z = L$, Eq. (10) can be used to compare the geometric glare point image to the diffraction spot. A non-dimensional parameter R_{GD} (ratio of geometric to diffraction diameters) is introduced:

$$R_{\text{GD}} = \frac{M\delta_g}{d_{\text{diff}}} = \frac{2 + \sqrt{2}}{8} (1+M) \frac{f}{Mz_0} \frac{d_b}{L}. \tag{11}$$

The physical interpretation of R_{GD} is that it indicates the optical regimes governed by diffraction ($R_{\text{GD}} \ll 1$) from those where the tracer image (or the reflecting region thereof) is resolved in its geometry ($R_{\text{GD}} \gg 1$). When $R_{\text{GD}} = o(1)$, both effects need to be contemplated and a possible combination is given by Eq. (9).

Large-scale PIV applications typically entail large distance from the object and $M \ll 1$. From the thin-lens equation, this implies $f \approx Mz_0$ and Eq. (11) simplifies into:

$$R_{\text{GD}} \approx 0.4 \frac{d_b}{L}. \tag{12}$$

For any meaningful large-scale volumetric PIV experiment the ratio $d_b/L \ll 1$ (typically $[10^{-2}-10^{-4}]$, see Table 1), in turn, indicating that $R_{\text{GD}} \ll 1$. It can be concluded that also for HFSB tracers the imaging process is governed by diffraction [Eq. (9)], contrary to what is stated on the reference literature and textbooks (Adrian 1991; Raffel et al. 2018), where an upper limit (around 10–100 μm) is postulated for the tracer size before the geometric optics imaging regime needs to be accounted for.

Another relevant parameter for the imaging of HFSB is the distance between the two glare points, d_g in object space, as sketched in Fig. 5. This distance depends on the tracer size and the illumination-imaging relative angle (β) as (Dehaeck et al. 2005):

$$d_g = \cos\left(\frac{\pi - \beta}{2}\right) d_b, \tag{13}$$

which, for $\beta = 90^\circ$, reduces to $d_g = \frac{\sqrt{2}}{2} d_b$. In the image plane, this distance transforms into Md_g . This can be further compared with the diffraction spot [Eq. (8)], thus defining

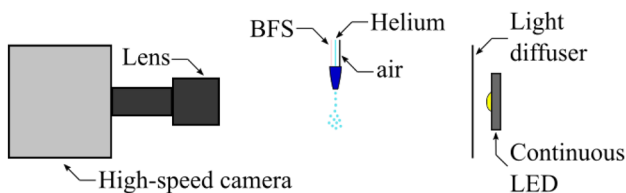


Fig. 6 Sketch of the experimental set-up for shadow visualization of the HFSB production

a new non-dimensional parameter, R_{DD} (ratio of glare point distance and diffraction diameter), as:

$$R_{\text{DD}} = \frac{Md_g}{d_{\text{diff}}} \approx 0.3 \frac{M}{f_{\#}} \frac{d_b}{\lambda_0}. \tag{14}$$

The physical interpretation of R_{DD} is that it indicates if the two glare points will be imaged separately ($R_{\text{DD}} \gg 1$) or will fall into the same diffraction spot ($R_{\text{DD}} \ll 1$). The former poses additional challenges to the triangulation and tracking of the tracers, as discussed by Faleiros et al. (2021). While the condition for diffraction-governed imaging is easily satisfied in volumetric PIV experiments [Eq. (12)], that for glare point merging is more restrictive and will further depend upon the imaging configuration [Eq. (14)]. Still, for large-scale experiments, where $M \ll 1$, this condition is easily satisfied as well.

The ratio R_{DD} is given in Table 1 for a series of relevant large-scale volumetric PIV experiments. In general, $R_{\text{DD}} < 1$ is observed. The condition $R_{\text{DD}} \ll 1$ (glare point merging) is more easily achieved when considering low values of β , as set when using the coaxial volumetric velocimeter (Jux et al. 2018; Schneiders et al. 2018). On the other hand, $R_{\text{DD}} \gg 1$ (separate glare points) brings the opportunity of triangulating tracers from single-camera approaches (Hou et al. 2021; Kaiser and Rival 2023).

3.4 HFSB sizing rules for large-scale PIV

As a result of the above discussion, the scattered light by HFSB tracers scales with the square of the bubble diameter. Furthermore, glare points imaging remains governed by diffraction and, when imaged at small magnification, both glare points fall within the diffraction spot. Introducing these results in Eq. (6), together with the depth of focus condition from Eq. (10) in the assumption of large-scale experiment the mean exposure $\bar{\varepsilon}$ reads as:

$$\bar{\varepsilon} \sim \frac{I_0 d_b^2}{L^4 M^2}. \tag{15}$$

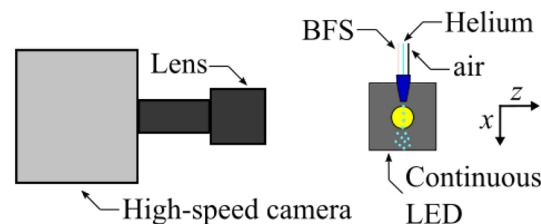


Fig. 7 Sketch of the experimental set-up for the light scattering investigation of scaled HFSB, using a viewing angle of 90° between the camera and the illumination source

Table 2 Imaging parameters for the light scattering experiment

Object distance (m)	0.2	0.53	1.16	2.21	5.36	10.61
Magnification	1.1	0.25	0.1	0.05	0.02	0.01
Pixel image size (μm)	18	80	200	400	1000	2000
f -number	2.8	8	8	8	8	8
Exposure (μs)	3	10.5	10.5	10.5	10.5	10.5

When the optical magnification is expressed as the ratio between the image and the object size ($M = s/L$), Eq. (15) can be rearranged to express the measurement size as a function of the other parameters:

$$L \sim \sqrt{\frac{I_0}{\epsilon}} \frac{d_b}{s}. \quad (16)$$

Equation (16) implies that, for a given level of illumination and sensor size and for a required exposure, the achievable volumetric measurement size scales linearly with the bubble diameter. This strong dependence motivates the exploration of the scalability of the tracers, such to match the needs of aerodynamics experiments for different purposes and scales. Furthermore, Eq. (16) is consistent with the slope of the linear trend in Fig. 1 for tracers scattering in the Mie regime (tracers larger than $1 \mu\text{m}$) and sets a benchmark for future large-scale volumetric PIV experiments.

4 Experimental set-up and procedures

4.1 HFSB generator

The bubble generator employed is based on a 3D-printed HFSB-GEN-V11 model, developed at TU Delft. The

generator is modified to feature a variable orifice diameter, while the geometry of the tri-axial duct and the contraction is left unaltered. The orifice diameter is changed by installing an adapted cap. Experiments cover a wide range of $d_o = \{0.35, 0.4, 0.5, 0.6, 0.75, 1, 1.5, 2, 2.5, 3\}$ mm. The lower limit of this interval is set by the achievable resolution of the 3D printer used (Anycubic Photon Mono X 6K), while the upper one is approaching the outer size of the generator itself, such that $d_{air}/d_o \sim 1$. Specific details on the geometry of the current generator are illustrated in “Appendix”.

The generator is supplied with pressurized air and helium. SAI 1035 fluid, from Sage Action, Inc. is used as BFS, with a surface tension of 27.5 mN/m . The air flow rate is set using a Festo SFAH mass flow controller, while the helium and BFS flow rates are set by imposing a known pressure ahead of previously calibrated flow resistors. At all flow rates, the neutrally buoyant nominal condition in ambient air is maintained by controlling $Q_{He}/Q_{BFS} \approx 1080$ (Faleiros et al. 2019). The flow rates vary from $Q_{He} = 2.2 \text{ l/h}$, $Q_{BFS} = 2 \text{ ml/h}$ and $Q_{air} = 15 \text{ l/h}$ for the smallest orifice to $Q_{He} = 30 \text{ l/h}$, $Q_{BFS} = 28 \text{ ml/h}$ and $Q_{air} = 230 \text{ l/h}$ for the largest one.

4.2 Bubble diameter and production rate

Shadow visualization is used to observe the production mechanism and infer bubble diameter and production rate,

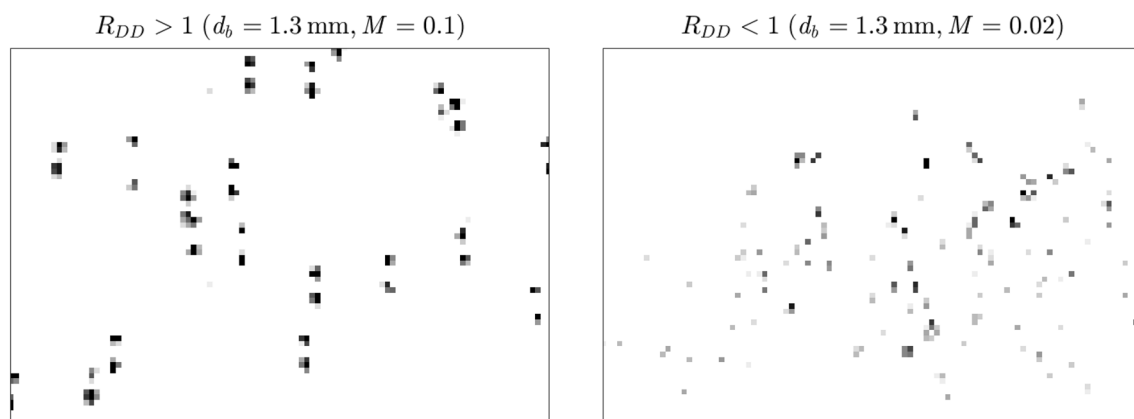


Fig. 8 Recordings of the light scattered by HFSB with a diameter of $d_b = 1.3 \text{ mm}$. Left: high optical magnification ($M = 0.1$), where the glare points are resolved separately ($R_{DD} > 1$). Right: typical optical magnification of PIV experiments ($M = 0.02$), where the glare

points merge onto a single pixel or within the diffraction diameter ($R_{DD} < 1$). A sequence of recordings obtained at 10 kHz is provided in the electronic supplementary material (Online Resource 1)

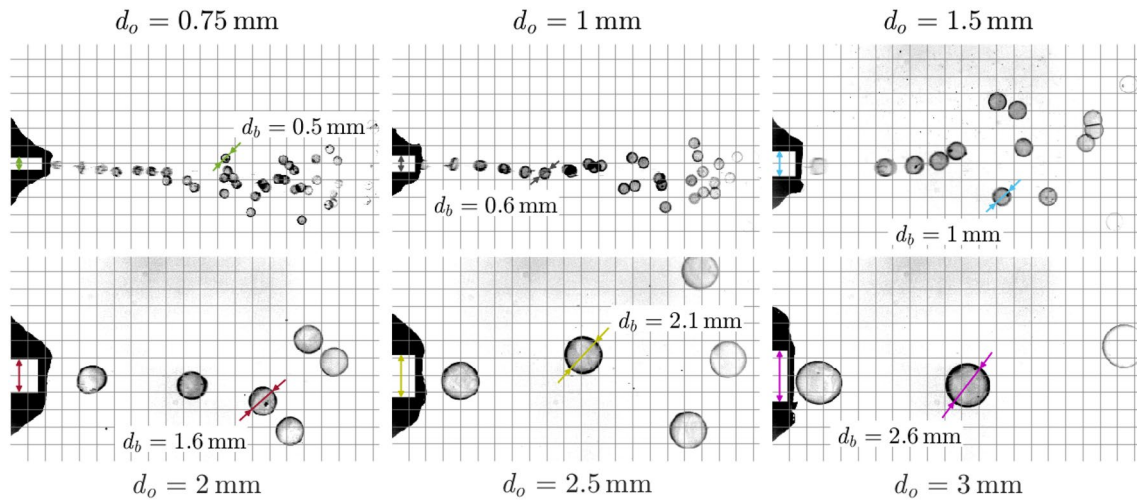


Fig. 9 Shadow visualization of HFSB produced varying the orifice diameter of the nozzle. Fluids flow rates are kept constant at $Q_{He} = 10$ l/h, $Q_{BFS} = 9.3$ ml/h and $Q_{air} = 100$ l/h. Reference grid with 1-mm

pitch. A time-resolved sequence of recordings acquired at 40 kHz is provided in the electronic supplementary material (Online Resource 2)

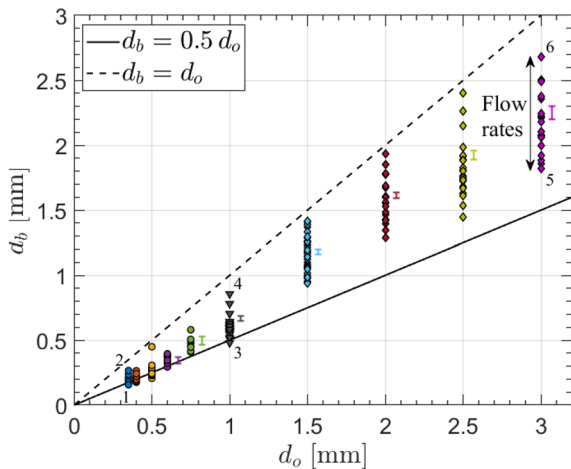


Fig. 10 HFSB diameter as a function of the orifice diameter, for every fluids flow rates combination

as sketched in Fig. 6. Continuous white light is provided by a LED (Scangrip Nova R, 2000 lm) along the region of interest (~ 20 mm at the exit of the generator), placed

behind a light diffuser. Images of the HFSB shadows are taken with a high-speed CMOS camera (Photron FASTCAM SA1.1, 1024×1024 px, 12 bits, $20 \mu\text{m}$ pixel pitch), placed perpendicular to the bubble stream and opposite to the illumination source, using a camera lens with $f = 105$ mm and setting $f_{\#} = 5.6$.

The production mechanism is inspected from a visualization with a digital imaging resolution of approximately 50 px/mm, cropping the sensor down to 320×128 px to achieve an acquisition frequency of 100 kHz. The imager is operated with a shutter of $8 \mu\text{s}$ to avoid motion blur. As discussed by Faleiros et al. (2019) and Gibeau et al. (2020), only specific combinations of the fluids flow rates result in a stable production of HFSB in the so-called *bubbling* regime. An in-house algorithm detects the bubbles of circular shape and counts the number of bubbles produced during an acquisition of 10 ms (1000 frames). Statistics on the diameter and production rate are based on a typical ensemble size of 300 bubbles.

Table 3 Fluids flow rates employed to obtain the HFSB diameters numbered in Fig. 10

Orifice diameter, d_o (mm)	0.35		1		3	
	1	2	3	4	5	6
Number label (see Fig. 10)						
Mean bubble diameter, d_b (mm)	0.16	0.27	0.48	0.86	1.82	2.68
Standard deviation of bubble diameter (mm)	0.01	0.01	0.01	0.02	0.11	0.15
Q_{He} (l/h)	2.2	2.8	9.4	9.9	22.0	30.0
Q_{BFS} (ml/h)	2.0	2.6	8.7	9.2	20.4	27.8
Q_{air} (l/h)	40	15	145	50	230	90

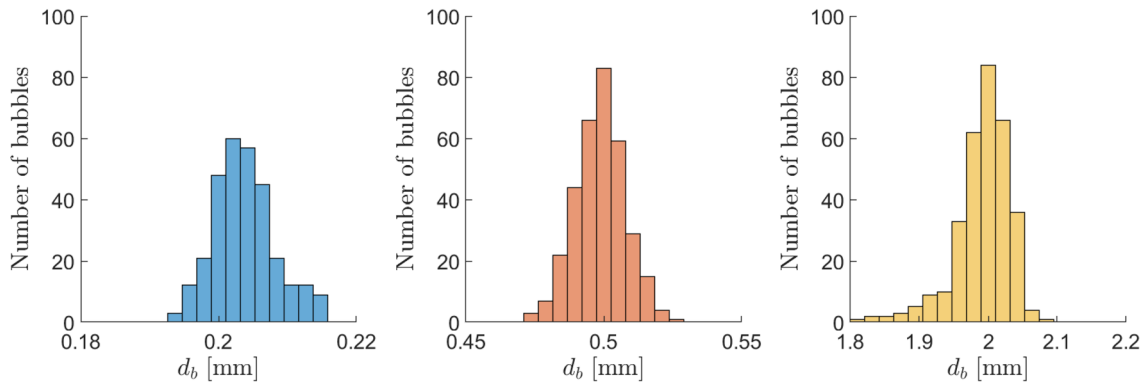


Fig. 11 Distribution of bubble diameter. Left: for a mean bubble diameter of 0.2 mm (obtained from $d_0 = 0.5$ mm). Middle: for a mean bubble diameter of 0.5 mm (obtained from $d_0 = 0.75$ mm). Right: for a mean bubble diameter of 2 mm (obtained from $d_0 = 3$ mm)

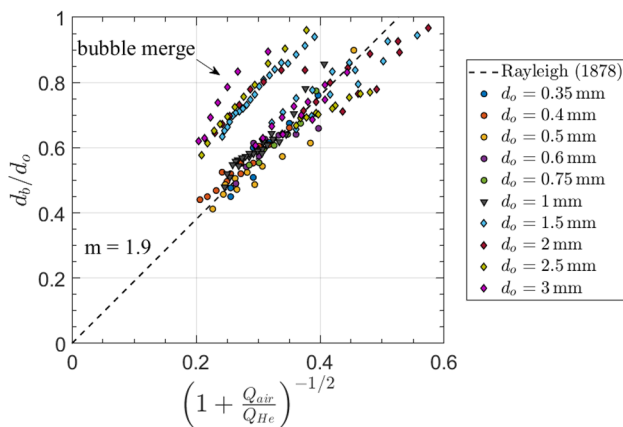


Fig. 12 Comparison between the experimental measurements of HFSB diameter and the theoretical prediction derived in Eq. (5)

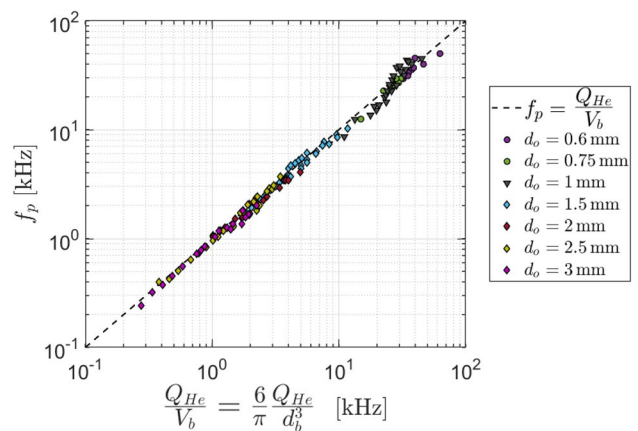


Fig. 13 HFSB production rate as a function of bubble diameter and helium flow rate imposed

4.3 Light scattering behaviour and glare points

Illumination and imaging directions are placed perpendicularly as shown in Fig. 7. The LED source is placed at a distance of approximately 10 cm from the generator’s exit and the light scattered by the HFSB is captured with the CMOS camera at a distance varying from 0.2 m up to 10 m. The goal of this experiment is to verify the power two scaling of scattered light with the bubble diameter and confirm the hypothesis of diffraction-dominated regime [$R_{GD} \ll 1$, Eq. (11)].

The experiments are conducted by varying both the bubble diameter and the optical magnification (see Table 2). The bubble diameter is varied by changing the generator orifice and controlling the fluids flow rates. The imaging distance is adjusted by moving the camera away from the generator. Furthermore, the aperture is varied through the f-number. The optical magnification is varied from $M = 0.01$, representative of large-scale applications, up to $M = 0.25$, more aligned with experiments at smaller laboratory scale.

In these cases, the f-number is set to $f_{\#} = 8$ (commonly employed for volumetric PIV) and the camera exposure time to $10.5 \mu\text{s}$. Some recordings are performed at high-magnification ($M = 1.1$), large aperture ($f_{\#} = 2.8$) and short exposure time ($3 \mu\text{s}$), to attain the condition $R_{GD} > 1$. The latter resembles more closely the study of Adrian and Yao (1985), conducted at $M = 1$ with varying $f_{\#}$. For HFSB, raising the f-number has a major impact on the relative importance of geometric imaging, as it not only increases the diffraction spot [Eq. (8)], but also decreases the perceived glare point size [Eq. (7)]. The list of imaging configurations explored is given in Table 2.

The condition $R_{DD} > 1$ [Eq. (14)], indicating that the glare points are imaged separately, is obtained for high magnifications and/or large bubbles. From these, the bubble diameter is estimated to be $\sqrt{2}$ times larger than the distance between them (Scarano et al. 2015), given the 90° viewing angle. An in-house algorithm matches neighbouring glare points corresponding to the same bubble and extracts the individual particle image diameters,

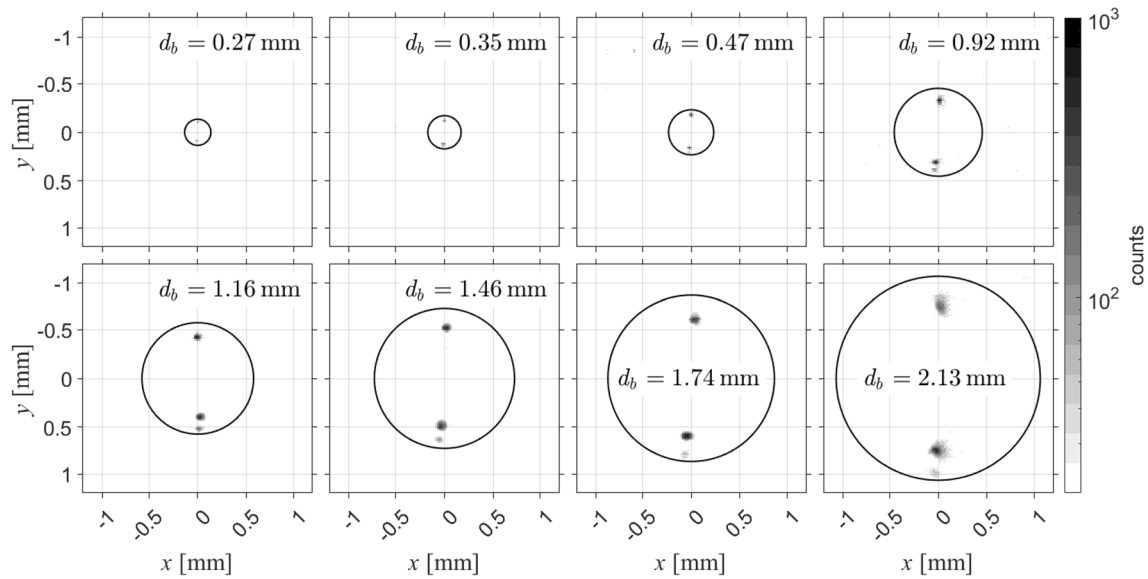


Fig. 14 High-magnification recordings ($M=1.1$) of the light scattered by HFSB of different diameter. The black circles indicate the estimated positions of the bubbles

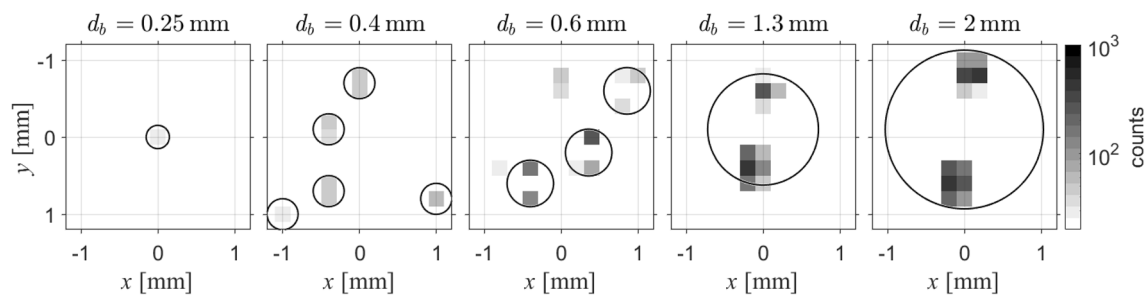


Fig. 15 Low-magnification recordings ($M = 0.1$) of the light scattered by HFSB tracers. The black circles indicate the estimated positions of the bubbles

peak intensity (indicative of particle detectability) and also integrates the intensity over the particle image region to obtain the total scattered light energy. Instead, for low magnifications and/or small bubbles, the two glare points merge in the image plane, and the algorithm is simply a peak finder that still computes the aforementioned properties for each bubble. Representative images of the regimes $R_{DD} > 1$ and $R_{DD} < 1$ are given in Fig. 8, obtained by decreasing the optical magnification from $M = 0.1$ to $M = 0.02$ for bubbles with a diameter of $d_b = 1.3$ mm.

For every imaging configuration listed in Table 2 and every bubble diameter considered, a total of 1000 snapshots are recorded. The particle image properties are obtained as the mean of all detected bubbles, after removing outliers using a third-order median filter. For the case of separate glare points, the intensity information from the two is added together, for a better comparison with the merged glare points situation. Uncertainty in the

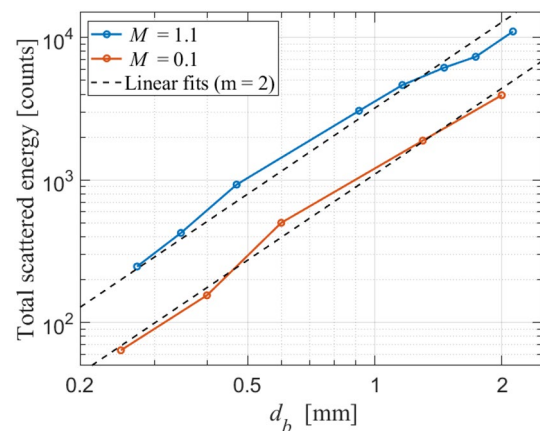


Fig. 16 Total scattered energy, integrated over the particle image diameter, for various HFSB diameters and two optical magnifications: $M = 1.1$ and $M = 0.1$

reported quantities is estimated as two times the standard deviation divided by the square root of the number of bubbles detected (Moffat 1988), which represents 95% confidence assuming a Gaussian distribution.

5 Results

5.1 Bubble production visualization

Changing the orifice diameter of the HFSB generator has a major impact on the size of the bubbles produced. Examples of the bubbles generated are given in Fig. 9 for six different orifice diameters. The shadow images are accompanied by a 1-mm grid to give a clear indication of the bubble size. Besides, the diameter of a specific bubble is also indicated for each case. For every orifice, the fluids flow rates are kept constant at $Q_{He} = 10$ l/h, $Q_{BFS} = 9.3$ ml/h and $Q_{air} = 100$ l/h. From the visualizations, it is apparent that HFSB can be produced within a range of diameters $d_b \in [0.5, 2.6]$ mm simply by changing the orifice diameter.

The complete set of bubble diameters measured from the shadow visualizations are given in Fig. 10 in terms of the orifice diameter, ranging from $d_b = 160 \mu\text{m}$ for $d_o = 0.35$ mm to $d_b = 2.7$ mm for $d_o = 3$ mm. For a chosen orifice, different bubbles can be generated by changing the air and helium relative flow rates, obtaining diameters roughly from $d_b = 0.5d_o$ up to $d_b = d_o$. While the upper limit is set by the orifice itself, it is argued that the lower limit is set by the maximum shear tolerated during the extrusion of the BFS film. The fluids flow rates combination employed to generate the HFSB diameters numbered in Fig. 10, which correspond to the minimum and maximum bubble diameters achieved for $d_o = 0.35$ mm, $d_o = 1$ mm and $d_o = 3$ mm are listed in Table 3. The error

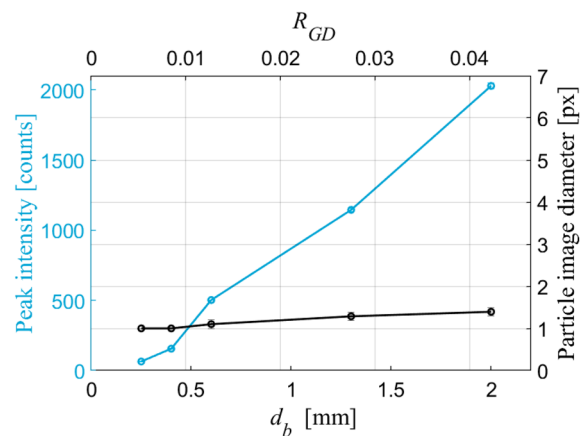


Fig. 18 Peak intensity and particle image diameter for various HFSB diameters imaged at $M = 0.1$ ($R_{GD} \ll 1$)

bars next to the symbols in Fig. 10 indicate the mean of the bubble diameter standard deviation measured for every fluid flow rates combination during the full acquisition. The obtained values are below 5% of the mean bubble diameter, in agreement with the results discussed by Faleiros et al. (2019) for stable production in the *bubbling* regime. The size dispersion is further illustrated in Fig. 11 by showing histograms of the measured bubble diameter distribution for three different situations: $d_b = 0.2$ mm, $d_b = 0.5$ mm and $d_b = 2$ mm.

The experimental measurements of the bubble diameter are further compared with the theoretical prediction derived in Eq. (5). The comparison is given in Fig. 12, where the theoretical trend is represented by a dashed line that goes through the origin with a slope equal to $m = 1.9$. This value results from assuming that the bubble production dominant wavelength is the same as the

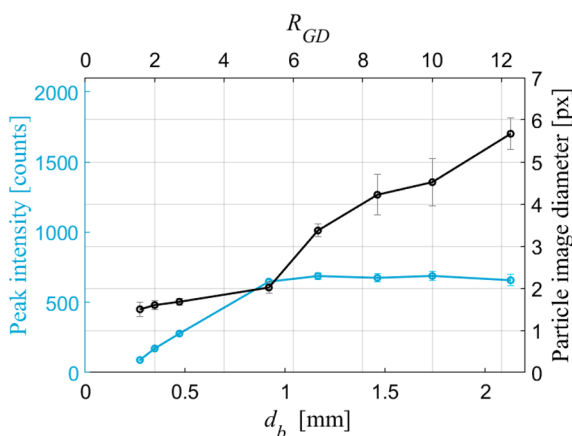


Fig. 17 Peak intensity and particle image diameter for various HFSB diameters imaged at $M = 1.1$ ($R_{GD} \geq 1$)

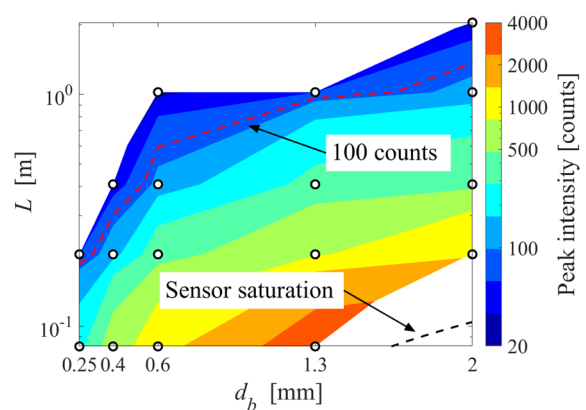


Fig. 19 Peak intensity (in logarithmic scale) for various HFSB diameters and measurement sizes. Values of L are based on the current choice of illumination and scale with the pulse energy of the source

one derived by Rayleigh (1878) for a cylindrical liquid jet in air. The experimental measurements are indicated by the scattered dots coloured by the orifice diameter, and in general are in good agreement with the theory. For $d_o \geq 1.5$ mm and low values of both Q_{He} and Q_{air} , an alternative regime is also observed that results in bigger bubbles than those predicted by Eq. (5) for the fluids flow rates imposed. Arguably, this is caused by the merging of two bubbles just ahead of the orifice, forming a bigger bubble downstream of the generator.

The high-speed shadow visualizations allow estimating the bubble production rate. Counting the number of bubbles crossing a line at a chosen distance from the exit delivers the results shown in Fig. 13. The data are compared with the prediction from Eq. (2), which imposes helium mass conservation. The production rate is plotted as a function of Q_{He} normalized with the bubble volume. The data exhibit linearity over a wide range, spanning from 250 Hz, obtained for the largest bubbles of approximately 3 mm, to 50 kHz for bubbles of 0.3 mm. Extrapolation of this behaviour to the smallest bubbles of 160 μm predicts a production rate in excess of 300 kHz. The latter could not be measured with the current apparatus, leaving the point open for further verifications. The measured production rate, in excess of $f_p = 10$ kHz for $d_o = 1$ mm, is in agreement with both Gibeau et al. (2020) and Faleiros et al. (2019).

5.2 Light scattering and HFSB imaging

The imaging regime of HFSB depends upon their size, the optical magnification and to a lesser extent it is affected by the relative angle between illumination and imaging direction. Figure 14 illustrates the images of HFSB obtained at relatively high magnification, ($M = 1.1$), for bubbles with diameter ranging from $d_b = 0.27$ mm to $d_b = 2.13$ mm. In this condition, the glare points are always imaged with two maxima separated by a distance (vertical, given the top-to-bottom illumination, Fig. 7), which suggests $R_{DD} > 1$. A third glare point, of weaker intensity is observed for the larger bubbles, caused by a higher order internal light reflection. Given its low intensity, the contribution of this glare point to the total scattered energy is neglected.

Reducing the optical magnification (see Table 2) to $M = 0.1$ and for bubble size ranging from $d_b = 0.25$ mm up to $d_b = 2$ mm (inferred from the glare points distance), Fig. 15 shows that the glare points merge into a single peak for the smaller bubbles ($R_{DD} < 1$), causing either an elongated particle image (for $d_b = 0.4$ mm), or a single pixel being activated (for $d_b = 0.25$ mm). In this case, both the geometric and diffraction contributions are smaller than the pixel pitch of 20 μm . Introducing the appropriate values into the theoretical estimations given in Eq. (7) and Eq. (8) returns a geometric glare point image size ($M\delta_g$) of only 0.05 μm . Comparatively, the diffraction spot is larger (approximately 12 μm), thus in agreement with the experimental evidence.

The information about the particle image size is further used to integrate the detected intensity level in this region, thus providing an estimate of the total light energy scattered by the HFSB. The results obtained for every bubble diameter considered are shown in Fig. 16 for the imaging configurations at $M = 1.1$ and $M = 0.1$. The experimental measurements, displayed in logarithmic scale, are further compared with linear trends with a slope of $m = 2$. This value responds to the power-law exponent of the geometric light scattering regime (Tropea 2011). It can be seen that this exponent matches well for both imaging situations, as the light scattered is a function of the particle diameter (relative to the incoming light wavelength) only.

The influence of the imaging configuration arises when looking at the particle image diameter and peak intensity, the latter being representative of particle detectability and therefore of great importance for PIV experiments. Starting with the high-magnification situation, $M = 1.1$, the obtained particle image diameter and peak intensity are given in Fig. 17 for the eight different HFSB diameters considered. As the bubble size increases, the peak intensity initially does also increase, before reaching a constant value for bubbles bigger than 1 mm. This is caused by the role of geometric optics on the particle image diameter of the glare points. While $R_{GD} = o(1)$, the contribution of diffraction and geometric imaging is comparable, and thus both peak intensity and particle image diameter increase. As $R_{GD} \gg 1$ for the bigger bubbles tested, diffraction becomes negligible

and the particle image size increases linearly with that of the bubble. This situation, originally discussed by Adrian (1991) to postulate an upper limit for the usable tracer size for PIV, has no implication for volumetric experiments, as can only be achieved for low f -numbers (decreasing the depth of focus) combined with big tracers and high optical magnifications.

Instead, for an imaging situation more representative of a large-scale volumetric PIV experiment, such as the one discussed above for $M = 0.1$, the evolution of peak intensity and particle image diameter as the tracer size is increased follows the pattern given in Fig. 18. Here, even if diffraction dominates over the geometric size ($R_{GD} \ll 1$), the particle image diameter is limited by the pixel pitch of the sensor. Only for bigger bubbles the high intensity peak makes the distribution spread slightly to neighbouring pixels, as can be seen in Fig. 15. According to Eq. (7), the HFSB would need to be bigger than 3 cm for its glare point to spread over more than a pixel in this configuration. As the particle image diameter remains nearly constant throughout the entire range, the peak intensity follows a quadratic relation with the bubble diameter, which maintains the quadratic relation for the total scattered energy discussed in Fig. 16. This means that, for practical applications, the tracer size can be increased to improve particle detectability. This may be used to better distinguish tracers over reflecting backgrounds or simply to scale the measurement size, as summarized in Eq. (16).

The peak intensity analysis is extended to other optical magnifications, as reported in Table 2. The measured intensity is shown in Fig. 19 for every combination of bubble diameter and measurement size ($L = s/M$) tested. The observed trend agrees well with the theoretical scaling derived in Eq. (16), which suggests an intensity increase for bigger bubbles and smaller measurement domains. The actual intensity values reported in Fig. 19 depend not only on the quantum efficiency of the sensor but also on the illumination and recording characteristics. For more general purposes, they could be scaled with respect to the 2000 lm illumination source placed at 10 cm from the tracers and exposed during $10.5 \mu\text{s}$.

6 Conclusions

The scalability of HFSB as tracers for volumetric PIV applications is explored by changing the orifice of the bubble generator and fluids flow rates. While keeping the nominal neutral buoyancy condition, bubble diameters between $160 \mu\text{m}$ and 2.7 mm have been produced. For every situation, the diameter dispersion is below 5% of the mean. As the bubble production frequency is inversely proportional to the bubble volume, production rates range from 250 Hz for the bigger bubbles to more than 300 kHz for the smaller ones. For a given geometry and fluids flow rates, the bubble diameter could be accurately predicted by imposing mass conservation and estimating the dominant wavelength of the bubble production instability mechanism.

The light scattering behaviour of the scaled HFSB has been investigated both from a theoretical and experimental perspective. While the size of HFSB translates into the geometric light scattering regime, it is demonstrated that, for large-scale volumetric PIV applications, the imaging conditions are such that the particle images are still well represented by the diffraction spot. This means that the bubble diameter can be further increased to produce brighter particle images, thus allowing for larger measurement volumes imaged from longer distances. It is postulated that $L \sim d_b$, which supports wide range scalability for volumetric PIV experiments.

Appendix: HFSB generator technical drawings

The design of the HFSB generator developed at TU Delft is manufactured with 3D printing. The technical drawings are included here, along with the corresponding stereolithography file (STL), to ease the reproduction of this critical component (Online Resource 3).

The generator comprises two parts: main generator and cap, connected with a thread. The main part features three inlets for the fluids (air, helium and BFS), which are arranged coaxially inside the generator, as described in Sect. 2. The second part (cap) sets the nozzle orifice diameter, d_o . The technical drawings of both parts contain the most relevant dimensions (Fig. 20). The geometry can be inspected in full details from the STL file.

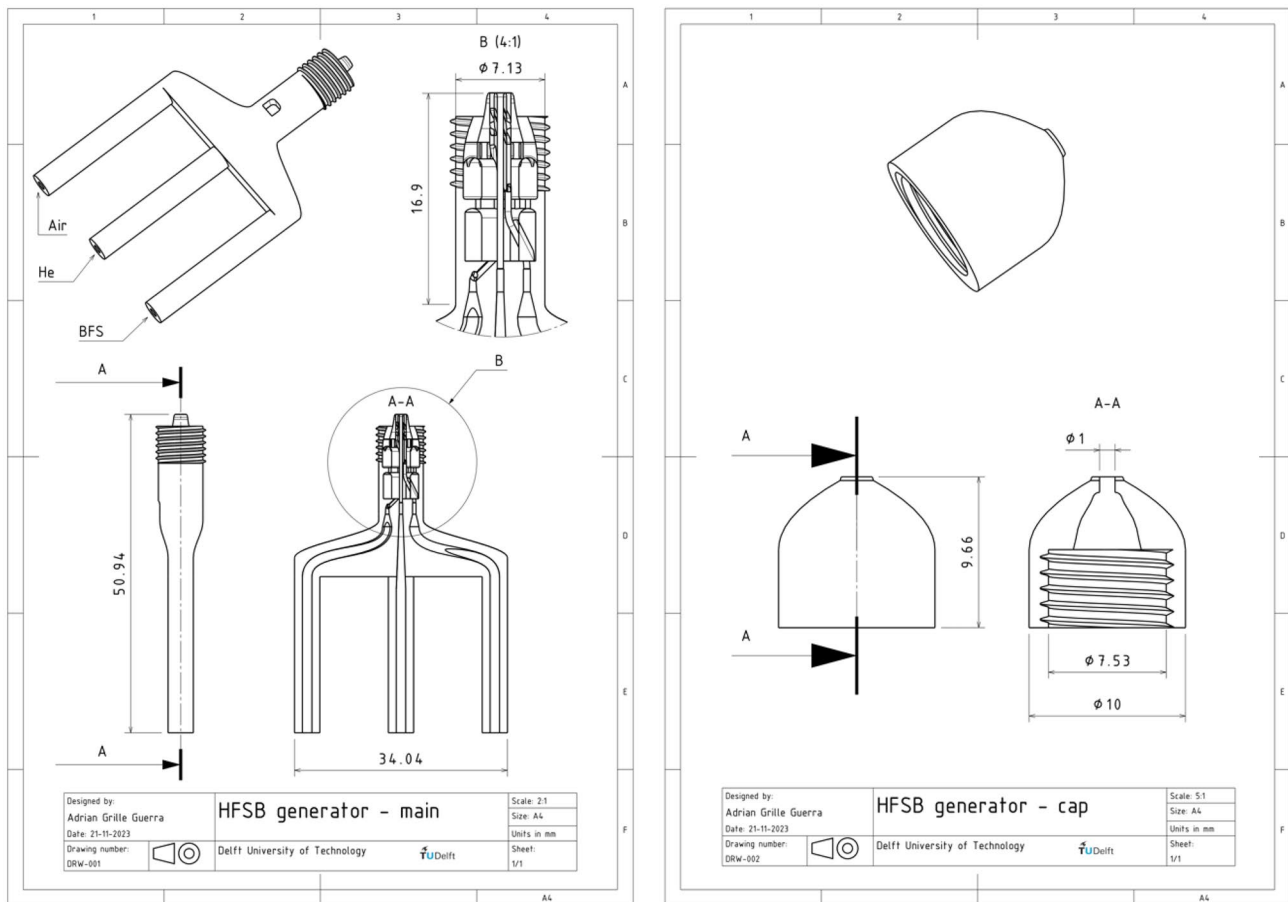


Fig. 20 HFSB generator main body cross sections (left) and detail of the generator cap, for $d_0 = 1$ mm. A stereolithography file (STL) of this design is provided in the electronic supplementary material (Online Resource 3)

Supplementary Information The online version contains supplementary material available at <https://doi.org/10.1007/s00348-024-03760-w>.

Author contributions All authors conceptualized and designed the experiments. A.G.G. conducted the experiments, analysed the results and prepared the manuscript draft. F.S. and A.S. reviewed the manuscript.

Funding Not applicable.

Availability of data and materials A digital version of the data presented in this publication can be found at <https://doi.org/10.4121/822fc9bb-7b03-4e16-8bef-1c5964ed9aa5>.

Declarations

Conflict of interest The authors declare no competing interests.

Ethical approval Not applicable.

Open Access This article is licensed under a Creative Commons Attribution 4.0 International License, which permits use, sharing, adaptation, distribution and reproduction in any medium or format, as long as you give appropriate credit to the original author(s) and the source, provide a link to the Creative Commons licence, and indicate if changes

were made. The images or other third party material in this article are included in the article's Creative Commons licence, unless indicated otherwise in a credit line to the material. If material is not included in the article's Creative Commons licence and your intended use is not permitted by statutory regulation or exceeds the permitted use, you will need to obtain permission directly from the copyright holder. To view a copy of this licence, visit <http://creativecommons.org/licenses/by/4.0/>.

References

- Adrian RJ (1991) Particle-imaging techniques for experimental fluid mechanics. *Annu Rev Fluid Mech* 23(1):261–304. <https://doi.org/10.1146/annurev.fl.23.010191.001401>
- Adrian RJ, Westerweel J (2011) Particle image velocimetry. Cambridge University Press, Cambridge
- Adrian RJ, Yao C-S (1985) Pulsed laser technique application to liquid and gaseous flows and the scattering power of seed materials. *Appl Opt* 24(1):44. <https://doi.org/10.1364/ao.24.000044>
- Atkinson C, Coudert S, Foucaut JM, Stanislas M, Soria J (2011) The accuracy of tomographic particle image velocimetry for measurements of a turbulent boundary layer. *Exp Fluids* 50(4):1031–1056. <https://doi.org/10.1007/s00348-010-1004-z>

- Barros DC, Duan Y, Troolin DR, Longmire EK (2021) Air-filled soap bubbles for volumetric velocity measurements. *Exp Fluids* 62(2):1–12. <https://doi.org/10.1007/s00348-021-03134-6>
- Bluyssen PM, Ortiz M, Zhang D (2021) The effect of a mobile HEPA filter system on ‘infectious’ aerosols, sound and air velocity in the SenseLab. *Build Environ* 188(2020):107475. <https://doi.org/10.1016/j.buildenv.2020.107475>
- Bosbach J, Kühn M, Wagner C (2009) Large scale particle image velocimetry with helium filled soap bubbles. *Exp Fluids* 46(3):539–547. <https://doi.org/10.1007/s00348-008-0579-0>
- Caridi GCA, Ragni D, Sciacchitano A, Scarano F (2016) HFSB-seeding for large-scale tomographic PIV in wind tunnels. *Exp Fluids* 57(12):1–13. <https://doi.org/10.1007/s00348-016-2277-7>
- Caridi GCA (2018) Development and application of helium-filled soap bubbles for large-scale PIV experiments in aerodynamics. Delft University of Technology. <https://doi.org/10.4233/uuid:effc65f6-34df-4eac-8ad9-3fdb22a294dc>
- Dehaeck S, Van Beeck JPAJ, Riethmuller ML (2005) Extended glare point velocimetry and sizing for bubbly flows. *Exp Fluids* 39(2):407–419. <https://doi.org/10.1007/s00348-005-1004-6>
- Elsinga GE, Scarano F, Wieneke B, Van Oudheusden BW (2006) Tomographic particle image velocimetry. *Exp Fluids* 41(6):933–947. <https://doi.org/10.1007/s00348-006-0212-z>
- Faleiros DE, Tuinstra M, Sciacchitano A, Scarano F (2018) Helium-filled soap bubbles tracing fidelity in wall-bounded turbulence. *Exp Fluids* 59(3):56. <https://doi.org/10.1007/s00348-018-2502-7>
- Faleiros DE, Tuinstra M, Sciacchitano A, Scarano F (2019) Generation and control of helium-filled soap bubbles for PIV. *Exp Fluids*. <https://doi.org/10.1007/s00348-019-2687-4>
- Faleiros DE, Tuinstra M, Sciacchitano A, Scarano F (2021) The slip velocity of nearly neutrally buoyant tracers for large-scale PIV. *Exp Fluids* 62(9):1–24. <https://doi.org/10.1007/s00348-021-03274-9>
- Faleiros DE (2021) Soap bubbles for large-scale PIV generation, control and tracing accuracy. Delft University of Technology. <https://doi.org/10.4233/uuid:c579128f-9e96-4e9e-9997-6ce9486e1e25>
- Gibeau B, Ghaemi S (2018) A modular, 3D-printed helium-filled soap bubble generator for large-scale volumetric flow measurements. *Exp Fluids* 59(12):1–11. <https://doi.org/10.1007/s00348-018-2634-9>
- Gibeau B, Gingras D, Ghaemi S (2020) Evaluation of a full-scale helium-filled soap bubble generator. *Exp Fluids* 61(2):1–18. <https://doi.org/10.1007/s00348-019-2853-8>
- Godbersen P, Bosbach J, Schanz D, Schröder A (2021) Beauty of turbulent convection: a particle tracking endeavor. *Physical Review Fluids* 6(11):110509. <https://doi.org/10.1103/PhysRevFluids.6.110509>
- Goodman JW (1996) Introduction to fourier optics, 2nd edn. McGraw-Hill
- Hale RW, Tan P, Stowell RC, Ordway DE (1971) Development of an integrated system for flow visualization in air using neutrally—buoyant bubbles. Issue SAI-RR 7107
- Hergert W, Wriedt T (2012) The Mie theory. In: Hergert W, Wriedt T (eds), vol 169. Springer, Berlin. <https://doi.org/10.1007/978-3-642-28738-1>
- Hou J, Kaiser F, Sciacchitano A, Rival DE (2021) A novel single-camera approach to large-scale, three-dimensional particle tracking based on glare-point spacing. *Exp Fluids*. <https://doi.org/10.1007/s00348-021-03178-8>
- Humble RA, Elsinga GE, Scarano F, van Oudheusden BW (2009) Three-dimensional instantaneous structure of a shock wave/turbulent boundary layer interaction. *J Fluid Mech* 622:33–62. <https://doi.org/10.1017/S0022112008005090>
- Huttig S, Gericke T, Sciacchitano A, Akkermans RAD (2023) Automotive on-road flow quantification with a large scale Stereo-PIV setup. In: Proceedings of the 15th international symposium on particle image velocimetry
- Jux C, Sciacchitano A, Schneiders JFG, Scarano F (2018) Robotic volumetric PIV of a full-scale cyclist. *Exp Fluids* 59(4):1–15. <https://doi.org/10.1007/s00348-018-2524-1>
- Kaiser F, Rival DE (2023) Large-scale volumetric particle tracking using a single camera: analysis of the scalability and accuracy of glare-point particle tracking. *Exp Fluids* 64(9):149. <https://doi.org/10.1007/s00348-023-03682-z>
- Kerho MF, Bragg MB (1994) Neutrally buoyant bubbles used as flow tracers in air. *Exp Fluids* 16(6):393–400. <https://doi.org/10.1007/BF00202064>
- Kühn M, Ehrenfried K, Bosbach J, Wagner C (2011) Large-scale tomographic particle image velocimetry using helium-filled soap bubbles. *Exp Fluids* 50(4):929–948. <https://doi.org/10.1007/s00348-010-0947-4>
- Moffat RJ (1988) Describing the uncertainties in experimental results. *Exp Thermal Fluid Sci* 1(1):3–17. [https://doi.org/10.1016/0894-1777\(88\)90043-X](https://doi.org/10.1016/0894-1777(88)90043-X)
- Mu K, Ding H, Si T (2020) Experimental and numerical investigations on interface coupling of coaxial liquid jets in co-flow focusing. *Phys Fluids*. <https://doi.org/10.1063/5.0002102>
- Percin M, van Oudheusden BW (2015) Three-dimensional flow structures and unsteady forces on pitching and surging revolving flat plates. *Exp Fluids* 56(2):1–19. <https://doi.org/10.1007/s00348-015-1915-9>
- Raffel M, Willert CE, Scarano F, Kähler CJ, Wereley ST, Kompenhans J (2018) Particle image velocimetry. In: *Handbuch Optische Messtechnik*. Springer. <https://doi.org/10.1007/978-3-319-68852-7>
- Rayleigh L (1878) On the instability of jets. In: Proceedings of the London Mathematical Society
- Rosi GA, Sherry M, Kinzel M, Rival DE (2014) Characterizing the lower log region of the atmospheric surface layer via large-scale particle tracking velocimetry. *Exp Fluids*. <https://doi.org/10.1007/s00348-014-1736-2>
- Scarano F (2013) Tomographic PIV: principles and practice. *Meas Sci Technol*. <https://doi.org/10.1088/0957-0233/24/1/012001>
- Scarano F, Poelma C (2009) Three-dimensional vorticity patterns of cylinder wakes. *Exp Fluids* 47(1):69–83. <https://doi.org/10.1007/s00348-009-0629-2>
- Scarano F, Ghaemi S, Caridi GCA, Bosbach J, Dierksheide U, Sciacchitano A (2015) On the use of helium-filled soap bubbles for large-scale tomographic PIV in wind tunnel experiments. *Exp Fluids*. <https://doi.org/10.1007/s00348-015-1909-7>
- Scarano F, Schneiders JFG, Gonzalez Saiz G, Sciacchitano A (2022) Dense velocity reconstruction with VIC—based time—segment assimilation. *Exp Fluids*. <https://doi.org/10.1007/s00348-022-03437-2>
- Schanz D, Novara M, Geisler R, Agocs J, Eich F, Bross M, Kähler CJ, Schröder A (2019) Large-scale volumetric characterization of a turbulent boundary layer flow. In: 13th international symposium on particle image velocimetry
- Schneiders JFG, Scarano F, Jux C, Sciacchitano A (2018) Coaxial volumetric velocimetry. *Meas Sci Technol*. <https://doi.org/10.1088/1361-6501/aab07d>
- Schröder A, Geisler R, Staack K, Elsinga GE, Scarano F, Wieneke B, Henning A, Poelma C, Westerweel J (2011) Eulerian and Lagrangian views of a turbulent boundary layer flow using time-resolved tomographic PIV. *Exp Fluids* 50(4):1071–1091. <https://doi.org/10.1007/s00348-010-1014-x>
- Schröder A, Schanz D, Bosbach J, Novara M, Geisler R, Agocs J, Kohl A (2022) Large-scale volumetric flow studies on transport of

- aerosol particles using a breathing human model with and without face protections. *Phys Fluids*. <https://doi.org/10.1063/5.0086383>
- Schuth M, Buerakov W (2017) Handbuch Optische Messtechnik. In: Handbuch Optische Messtechnik, 3rd edn. Carl Hanser Verlag GmbH & Co. KG. <https://doi.org/10.3139/9783446436619>
- Spoelstra A, de Martino Norante L, Terra W, Sciacchitano A, Scarano F (2019) On-site cycling drag analysis with the Ring of Fire. *Exp Fluids* 60(6):90. <https://doi.org/10.1007/s00348-019-2737-y>
- Tokgoz S, Elsinga GE, Delfos R, Westerweel J (2020) Large-scale structure transitions in turbulent Taylor-Couette flow. *J Fluid Mech*. <https://doi.org/10.1017/jfm.2020.679>
- Tropea C (2011) Optical particle characterization in flows. *Annu Rev Fluid Mech* 43:399–426. <https://doi.org/10.1146/annurev-fluid-122109-160721>
- van der Hoek D, Frederik J, Huang M, Scarano F, Simao Ferreira C, Van Wingerden JW (2022) Experimental analysis of the effect of dynamic induction control on a wind turbine wake. *Wind Energy Sci* 7(3):1305–1320. <https://doi.org/10.5194/wes-7-1305-2022>
- van Hout R, Hershkovitz A, Elsinga GE, Westerweel J (2022) Combined three-dimensional flow field measurements and motion tracking of freely moving spheres in a turbulent boundary layer. *J Fluid Mech* 944:1–39. <https://doi.org/10.1017/jfm.2022.477>
- Wei NJ, Brownstein ID, Cardona JL, Howland MF, Dabiri JO (2021) Near-wake structure of full-scale vertical-axis wind turbines. *J Fluid Mech* 914:1–40. <https://doi.org/10.1017/jfm.2020.578>
- Westerweel J, Elsinga GE, Adrian RJ (2013) Particle image velocimetry for complex and turbulent flows. *Annu Rev Fluid Mech* 45:409–436. <https://doi.org/10.1146/annurev-fluid-120710-101204>

Publisher's Note Springer Nature remains neutral with regard to jurisdictional claims in published maps and institutional affiliations.